



**HAL**  
open science

## Ultrafast high-temperature sintering (UHS) of ZrB<sub>2</sub>-based materials

Emanuele de Bona, Charles Manière, Vincenzo Sglavo, Mattia Biesuz

► **To cite this version:**

Emanuele de Bona, Charles Manière, Vincenzo Sglavo, Mattia Biesuz. Ultrafast high-temperature sintering (UHS) of ZrB<sub>2</sub>-based materials. *Journal of the European Ceramic Society*, inPress, 44 (1), pp.567-573. 10.1016/j.jeurceramsoc.2023.09.007 . hal-04208347

**HAL Id: hal-04208347**

**<https://hal.science/hal-04208347v1>**

Submitted on 15 Sep 2023

**HAL** is a multi-disciplinary open access archive for the deposit and dissemination of scientific research documents, whether they are published or not. The documents may come from teaching and research institutions in France or abroad, or from public or private research centers.

L'archive ouverte pluridisciplinaire **HAL**, est destinée au dépôt et à la diffusion de documents scientifiques de niveau recherche, publiés ou non, émanant des établissements d'enseignement et de recherche français ou étrangers, des laboratoires publics ou privés.

# Ultrafast high-temperature sintering (UHS) of ZrB<sub>2</sub>-based materials

Emanuele De Bona<sup>a,#</sup>, Charles Manière<sup>b</sup>, Vincenzo M. Sglavo<sup>a</sup>, Mattia Biesuz<sup>a</sup>

<sup>a</sup> Department of Industrial Engineering, University of Trento, Via Sommarive 9, 38122 Trento, Italy

<sup>b</sup> CRISMAT, Normandie Univ, ENSICAEN, UNICAEN, CNRS, Caen, 14000, France

<sup>#</sup> Corresponding author: [emanuele.debona@unitn.it](mailto:emanuele.debona@unitn.it)

## Abstract

ZrB<sub>2</sub> is one of the most promising materials for extreme environment applications, especially in the aerospace field, due to the combination of superior thermophysical properties and low density. Nevertheless, pure ZrB<sub>2</sub> is intrinsically hard to sinter, requiring either the application of intense external pressure or the use of sintering aids.

In the present work, the feasibility of ultrafast high-temperature sintering (UHS) for the densification of commercial ZrB<sub>2</sub> was explored. Thanks to the addition of B<sub>4</sub>C as a sintering aid, Densities up to 92-98% could be obtained in just 2 min. Hardness of 16.3-17.8 GPa was obtained for the UHS ZrB<sub>2</sub>-based ceramics, similar to what is reported in the literature using slower, more sophisticated and energy-consuming sintering approaches like spark plasma sintering. These first results show that UHS could provide a quick and simple way to produce high-performance ZrB<sub>2</sub>-based components with just a few minutes of processing time in pressure-less conditions.

## 1. Introduction

Transition metals diborides (such as  $TiB_2$ ,  $ZrB_2$  and  $HfB_2$ ) are characterized by high melting temperature combined with excellent mechanical and physical properties (high thermal and electrical conductivity, chemical inertness against molten metals and great thermal shock resistance) [1–3]. These compounds belong to the group of Ultra-High-Temperature-Ceramics, a class of materials suitable for extreme applications such as high-temperature electrodes, crucibles for molten metal and structural or thermal protection components for hypersonic flight vehicles. Among them,  $ZrB_2$  is characterized by the lowest density, making it the best candidate for aerospace applications.

Nonetheless, the widespread use of  $ZrB_2$  has been limited by the difficulty in obtaining dense ceramic parts, due to its intrinsic low sinterability. This originates from the strong covalent bonding of  $ZrB_2$ , which results in limited self- and grain boundary diffusion coefficients. Moreover, the presence of oxides ( $B_2O_3$  and  $ZrO_2$ ) on the particle surfaces promotes coarsening over sintering at temperatures below which considerable densification can take place.[4]

Therefore, a combination of high sintering temperature and applied pressure is needed for producing dense  $ZrB_2$  components, like in hot pressing (HP).[1,5] Typically, temperatures above  $2000^\circ C$  and pressures above 30 MPa are needed to exceed a final relative density of 95%.[1,6,7] Similar results can be obtained by spark plasma sintering (SPS)[8] and flash spark plasma sintering (FSPS)[9]. However, all these techniques are limited to produce specimens of relatively simple shapes. In order to achieve comparable densities via pressureless sintering, the starting  $ZrB_2$  powder has to be milled and/or mixed with sintering aids. Ball milling of the commercial powders effectively enhances sinterability by lowering the particle size, but quickly wears the milling balls making it relatively expensive (frequent replacement of expensive carbide balls) and contaminating the original powder [2,10,11]. The advantages of the particle size reduction through ball milling, therefore, overlap with those of doping: the addition of compounds reacting with the oxide surface layer, such as WC (used as typical milling media),  $B_4C$  and C, results in the removal of these oxides and in the effective densification of  $ZrB_2$  without the application of external pressure [11–14]. In particular, the additions of WC and  $B_4C$  were shown to give further advantages to the final  $ZrB_2$ -based composites: the

inclusion of W improves the oxidation resistance of ZrB<sub>2</sub>[1], while the addition of B<sub>4</sub>C results in better final mechanical properties[12,15] and lighter components (thanks to the low density of B<sub>4</sub>C) which is of pivotal relevance in aerospace applications. Another strategy is the activation of liquid phase sintering by the addition of liquid phase formers, such as MoSi<sub>2</sub>[16], or low melting temperature transition metals (Cr, Fe, Ni)[17,18]. Overall, the addition of B<sub>4</sub>C yields multiple advantages thanks to the eutectic at 2200 ± 20°C in the Zr – B – C phase diagram [19,20].

The high temperatures required in said processes can be reached also using ultrafast high-temperature sintering (UHS), a recently developed technique allowing the densification of ceramic samples within a couple of minutes [21]. In brief, green components are placed within a graphite felt that is Joule heated by a current flow, reaching temperatures exceeding 2000°C with heating rates in the order of 10<sup>3</sup> K min<sup>-1</sup>. This technique enables the densification of specimens even with complex shapes, by using a relatively simple setup if compared to SPS or FSPS. So far it has been applied to different oxide systems [22–31], glasses[32], carbides [33,34], nitrides [35] and high-entropy borides[36].

The present work aims at exploring the applicability of ultrafast high-temperature sintering for the consolidation and densification of ZrB<sub>2</sub> with and without the addition of B<sub>4</sub>C as a sintering aid.

## 2. Experimental procedure

### Sample preparation

The ZrB<sub>2</sub> powder used in this work was acquired from Höganäs (Grade B, D<sub>50</sub> = 1.5–3 μm, containing Fe and Hf impurities and max 1.5% O). Samples of about 225 mg of powder were uniaxially pressed into green disks (diameter = 6 mm) under 500 MPa, resulting in a thickness of 2 mm (green relative density ≈ 60%). In order to increase the final density of the sintered material, some of the original ZrB<sub>2</sub> powder was mixed with 10 wt% B<sub>4</sub>C (TETRABOR® 3000F by ESK Ceramics GmbH, particle size around 0.8 μm). A batch of 10 g of composite powder was mixed for 30 min in ultrasonic bath with the addition of 10 mL of Methyl ethyl ketone as solvent, and the resulting slurry was dried overnight at 150°C. Considered the lower density of B<sub>4</sub>C with

respect to  $\text{ZrB}_2$  (2.52 and 6.09 g cm<sup>-3</sup> respectively), the mass of the  $\text{ZrB}_2\text{-B}_4\text{C}$  composite disks was lowered to 200 mg to preserve the same volume of the green disks under the same pressing conditions.

UHS was performed using a 6 x 16 x 73 mm<sup>3</sup> (thickness x width x length) graphite felt (Sigratherm® GFA), leaving 23 mm of span between the electrodes. Based on our previous tests, such dimensions were chosen so to have a relatively homogeneous temperature profile in the position of the sample. A larger span between the electrodes would increase the voltage needed for the process without improving much the temperature homogeneity and the maximum temperature in the sample region. As can be seen in the scheme reported in **Figure 1A**, 2 x 25 mm of felt were needed at the electrodes, leading to the total length of 73 mm. The samples were placed in the middle of the felt by opening a hole roughly of the same size of the green disks. All treatments were performed under Ar atmosphere. The current was applied using a Agilent 6674A power supply limited to a maximum of 35 A in current and 60 V in voltage. Considering the low sinterability of  $\text{ZrB}_2$ , only the most extreme sintering conditions were applied, namely 32 A and 35 A, with holding times from 15 s to 120 s. In all the experiments, the power source worked in current control mode, the applied voltage being always lower than the set voltage limit. Higher temperatures could be reached by decreasing the cross section of the graphite felt, thus increasing the current density. However, some tests performed with a 11 mm wide felt showed no improvement in the final density, while resulted in less reproducible samples (less error margin for the placement of the sample in the felt) and quicker degradation of the graphite.

### UHS thermal model

The UHS setup used in this work does not allow the measurement of the exact temperature reached by the sample within the graphite felt; for this reason it was calculated by finite elements modeling (FEM). The felt conductivity and specimen convection heat losses were calibrated by melting some known pure compounds (Cu, Ni, Pt). Small specimens were placed inside and above the felt, and a sequence of treatments was performed by gradually increasing the input current until melting of the specimens occurred. The input voltage was also measured with a Keithley 2100 multimeter directly on the extremes of the felt, in order to account for the losses due to the wires. These parameters are detailed in a previous work<sup>(article under review)</sup>. The

simulation focussed on the  $\text{ZrB}_2/10 \text{ wt\% B}_4\text{C}$  composite, whose electro-thermal properties were extracted from closest composite properties available in the literature and reported in **Table 1**. The simulated felt configuration can have a high impact on the effective temperature of the specimen. Depending on the experimental conditions, the electrical current distribution, the contact with the felt, the surface to surface thermal exchanges and the heat removal by convection (chimney effect) can also influence the specimen temperature. Consequently, three different configurations were considered, detailed and justified in the Results and discussion section. The first configuration is the heating of the felt without the sample, the second assumes that the sample surfaces are completely in contact with the felt, while in the latter there is no contact with the felt. The last configuration (“minimum contact”) simulates the experimental case where the irregular shape of the felt implies contact points and convection heat losses. These three configurations are reported in the in **Figure 1A**. The simulated current lines in **Figure 1B** show the electric current concentration in full-contact configuration and the regular deviation of the current lines in the “minimum contact” configuration.

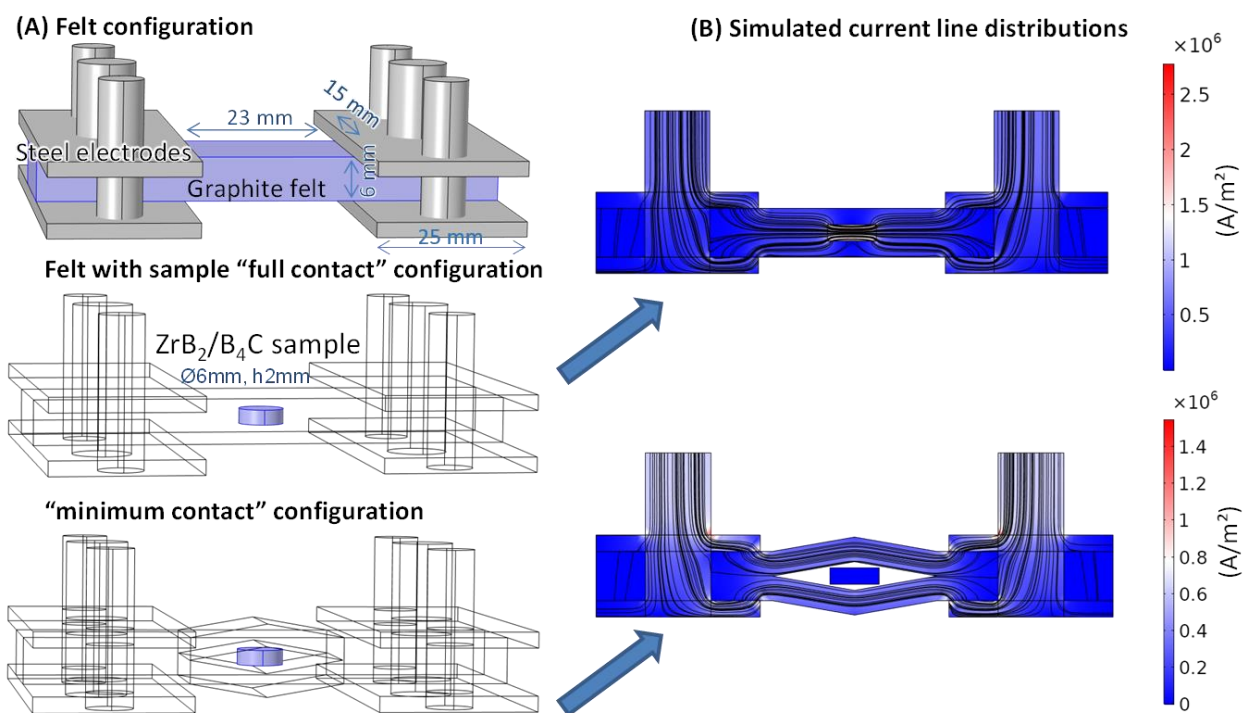


Figure 1: (A) Scheme of the three simulated configurations with the main felt and sample dimensions and (B) simulation of the current line distributions in the “full contact” and “minimum contact” configurations showing different electrical current flow.

Table 1: Electro-thermal properties of ZrB<sub>2</sub>-B<sub>4</sub>C composite

Property	Units	Value / dependence on temperature
Thermal conductivity of ZrB <sub>2</sub> -5wt%B <sub>4</sub> C[37]	W m <sup>-1</sup> K <sup>-1</sup>	4.37E-06T <sup>2</sup> – 1.68E-02T + 8.27E+01
Specific heat capacity of ZrB <sub>2</sub> -5wt%B <sub>4</sub> C[37]	J kg <sup>-1</sup> K <sup>-1</sup>	1.85E+02ln(T) – 5.57E+02
Electrical resistivity of ZrB <sub>2</sub> [38]	S m <sup>-1</sup>	1/((7.8+0.01(T-298))E-08)
Density of ZrB <sub>2</sub> [38]	kg m <sup>-3</sup>	6100
Emissivity of ZrB <sub>2</sub> [39]	-	0.9

## Characterization

The real density of the compounds was measured by He pycnometry using a Micromeritics AccuPyc 1330TC instrument (Micromeritics Instrument Corp., Norcross, GA, USA) on pure powders and on the ZrB<sub>2</sub>-B<sub>4</sub>C mixture. The apparent density of the sintered samples was measured by Archimedes' method according to the ASTM C 830 standard, thus allowing to calculate the relative density.

The microstructural characterization was performed both on polished and fracture surfaces by using a JEOL model JSM-5500 scanning electron microscope (SEM). The samples did not require metallization before analyses due to the conductive nature of ZrB<sub>2</sub>. Energy-dispersive X-ray spectroscopy (EDXS) was carried out separately on a JEOL JSM-IT300 LW equipped with a Bruker XFlash 630M detector operating at 20 keV.

X-ray diffraction (XRD) was performed on polished surfaces using a Rigaku IIID Max diffractometer, equipped with Cu-K $\alpha$  ( $\lambda = 1.5405 \text{ \AA}$ ) X-ray source (40 kV; 30 mA). The diffraction patterns were fitted using the crystallographic data provided by Mandal et al.[40] with the software package Jana2006[41].

Vickers hardness was measured using Future-Tech FM-310 microhardness tester and load of 9.8 N; the values presented in this work are the averages of 10 measurements per sample. The samples were preliminarily embedded in resin and then polished using SiC grinding papers (up to grit 4000).

### 3. Results and discussion

**Figure 2** shows the relative density of the different samples as a function of the UHS treatment time and current. The consolidation of pure  $ZrB_2$  powder is clearly limited, the relative density not exceeding 86%. Nevertheless, such value appears remarkable considering the ultra-refractory nature of the compound, the extremely limited treating time, the relatively large particle size and the absence of any sintering additive. The result is somehow promising as it shows that densification can take place in pressureless conditions using UHS. For comparison, Fahrenholtz et al. [15] reported densities limited to only 78% for commercial  $ZrB_2$  powder after 2 h sintering at 2100°C. The relatively good densification achieved by UHS might be a result of the rapid heating schedule, which was shown to be beneficial for the densification in many ceramic systems[42–46] as it favors densification over grain coarsening. An increase of the UHS current (from 32 to 35 A) does not affect substantially the final density (i.e., after 120 s), although densification is clearly anticipated, i.e., pure  $ZrB_2$  reaches a relative density of 84 % and xxx after 60 s under 35 and 32 A, respectively. On the other hand, sintering under the maximum current (35 A) results in coarser microstructure, as shown in **Figure 3**, where the coarsening phenomena are probably promoted by the residual surface oxide layer as it has been already reported in SPS [8].

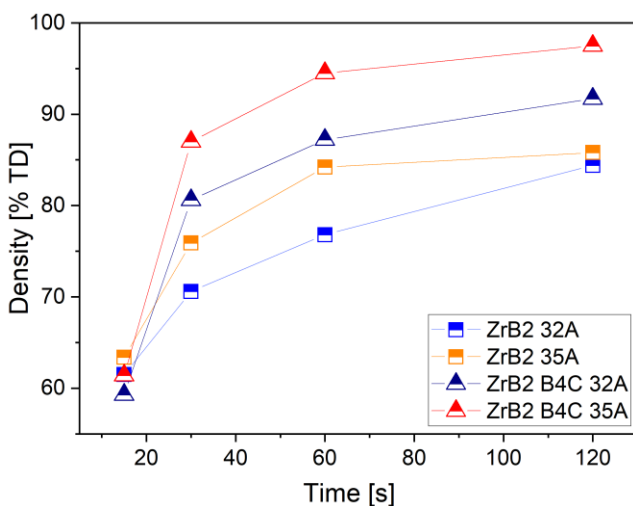


Figure 2: Relative density of  $ZrB_2$  and  $ZrB_2$ - $B_4C$  samples as a function of UHS holding time

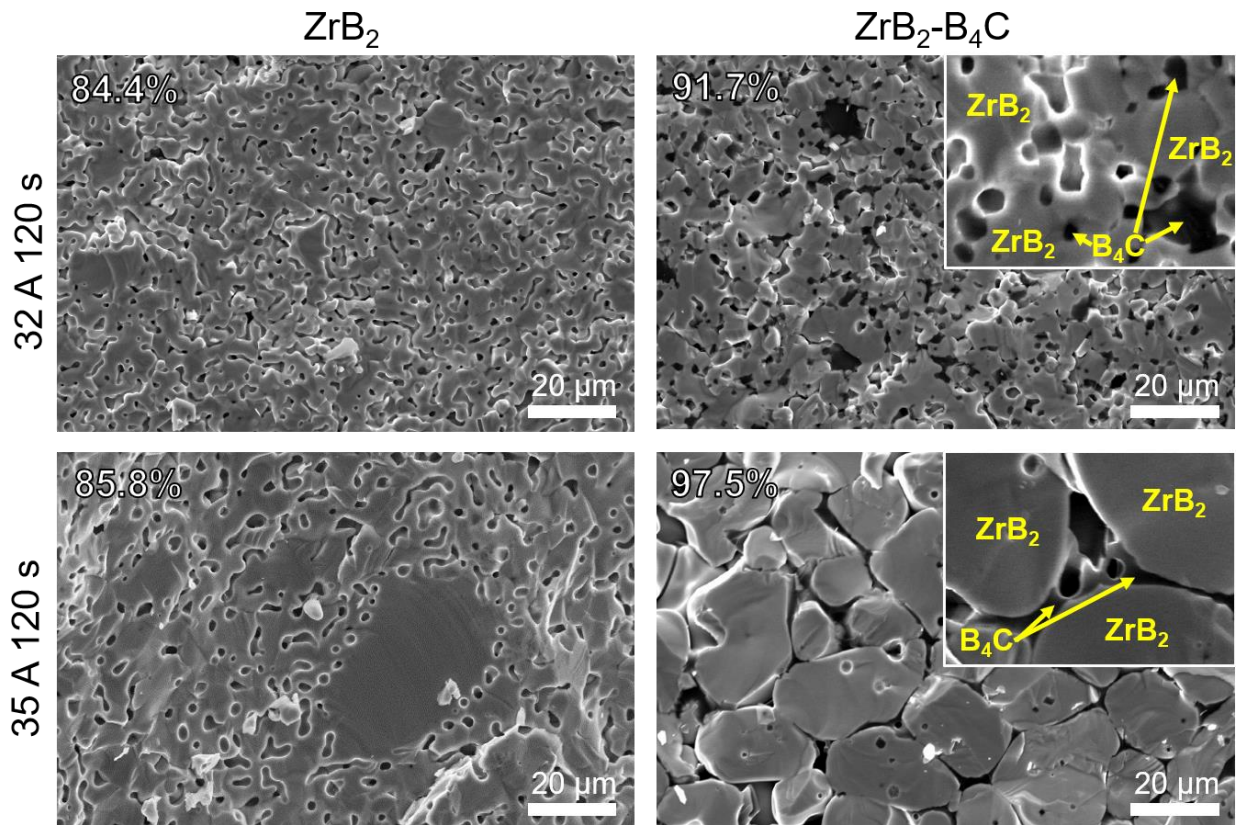


Figure 3: SEM micrographs of fresh fracture surfaces of the densest  $ZrB_2$  and  $ZrB_2-B_4C$  samples (produced with holding times of 120 s).

$B_4C$  addition causes a substantial densification improvement by a two-fold mechanism that can be appreciated by analyzing the density data in **Figure 2** and the micrographs in **Figure 3** (additional micrographs are available in **Figure S1-S5** of the Supplementary material). At 32 A for 120 s, the  $ZrB_2-B_4C$  composite reached a density of 91.7%, while undergoing only limited coarsening if compared to the pure  $ZrB_2$  sample produced in the same conditions (top row of **Figure 3**). No evidence of  $B_4C$  melting can be observed in the micrographs, where  $B_4C$  equiaxial grains appear to be distributed within the  $ZrB_2$  matrix. The improved densification can be then attributed to the removal of the surface oxides of the as-purchased  $ZrB_2$  powder by solid-state reaction with  $B_4C$ , as already documented by other authors [11,12,14].

By increasing the current from 32 A to 35 A, the final density increases further, reaching 94.5% after 60 s and 97.5% after 120 s, this being due to a variation in the sintering mechanism. In such condition, the temperature is also high enough to melt  $B_4C$  inducing liquid phase sintering and quicker densification.  $B_4C$  melting is supported by clear microstructural evidences (**Figure 3**). In particular, round-edged grains usually associated

with liquid phase sintering[47] can be appreciated. The rounded grain shape is consistent with their growth by Ostwald ripening within an isotropic (liquid) matrix, without any clear evidence of equilibrium triple points at the  $ZrB_2$ - $B_4C$  interface that would be expected for solid-state sintering. Moreover, the carbide phase (dark region of the micrograph) becomes interconnected and located at the grain boundaries between the boride grains as a result of an efficient wetting process (**Figure 3** and higher magnification micrographs in **Figure S4**). It is worth noting that, while pure carbide melts at about 2350°C, the  $ZrB_2$ - $B_4C$  system presents a eutectic at a significantly lower temperature (just above 2200°C)[40,48]. The solidification microstructures observed in this work do not support the eutectic formation as the typical lamellas formed during solidification were only very sporadically and locally observed (**Figure S6**). In general, the microstructural evidences back the hypothesis that liquid phase did not reach the eutectic composition (about 35 mol% of  $ZrB_2$ ).

When liquid phase sintering is active, the accelerated densification is a result of a generalized faster mass transport through the grain boundary liquid film. As such, not only densification but also grain coarsening takes place in a matter of seconds. The microstructure obtained after 2 min, therefore, consists of large boride grains whose size is in the order of 30  $\mu m$ . While exaggerated grain coarsening is in many cases undesired, in some applications of interest for  $ZrB_2$  it could be beneficial since, for instance, large-grained materials typically exhibit higher creep resistance [49].

The absence of secondary phase formation during the high-temperature treatment was verified by XRD on all samples, both pure  $ZrB_2$  and  $ZrB_2$ - $B_4C$  composites (**Figure S7**, Supplementary materials). The patterns show the presence of only  $ZrB_2$  crystalline phase ( $a = b = 3.169 \text{ \AA}$ ,  $c = 3.531 \text{ \AA}$ ;  $\alpha = \beta = 90^\circ$ ,  $\gamma = 120^\circ$ ) in good agreement with the literature, where the presence of  $B_4C$  is reported to be observable by XRD only for concentrations in excess to 20 wt%.[40,48]

FEM simulation was carried out to estimate whether the temperature reached during UHS could reasonably lead to  $B_4C$  melting. **Figure 4** shows that the maximum felt temperature and the average sample temperature, as well as the duration of the transient before reaching the temperature plateau, are affected by the considered configuration. In all conditions, the felt reaches the maximum temperature very quickly (less than 20 s in the worst case), while the temperature in the sample increases more slowly and stabilizes only after

20-30 s (heating rate  $\approx 4000\text{-}7000^\circ\text{C min}^{-1}$ ). This seems in good agreement with the fact that no substantial densification was observed in all cases after 15 s treatment (**Figure 2**). The system modeled with the presence of a hole around the sample shows lower temperatures for both the sample and the felt, due to the heat losses by convection and radiation.

To understand which modelled configuration represents more closely the real case, a calibration test was performed. A pure  $\text{B}_4\text{C}$  sample ( $T_m \approx 2350^\circ\text{C}$ ) was treated under 35 A for 120 s and it melted. The real temperature in the sample position might therefore slightly exceed that of the full contact model ( $2333^\circ\text{C}$ ). This simple test also backs up the possibility of having pure  $\text{B}_4\text{C}$  as liquid phase at 35 A. At 32 A for 120 s,  $\text{B}_4\text{C}$  did not melt, meaning the sample temperature did not reach  $2350^\circ\text{C}$ , in agreement with the “full contact” model (sample temperature around  $2236^\circ\text{C}$ ). In summary, the FEM simulations suggest that the UHS conditions can actually approach the melting point of pure boron carbide without the need for an eutectic reaction, this being quite in agreement with the microstructural evidence. A further hint towards the absence of any massive eutectic liquid formation comes from the sample treated at 32 A. It is worth remembering that the sample temperature at 32 A should also exceed that of the  $\text{ZrB}_2\text{-B}_4\text{C}$  eutectic (but not that of pure  $\text{B}_4\text{C}$ ), however no evidence of massive liquid phase sintering can be found in this sample. If the liquid phase present during sintering at 35 A were some eutectic composition, it should have occurred probably also during sintering at 32 A. The absence of an equilibrium eutectic liquid might be related to the fast treatment, in this regard, further investigation will be carried out in the near future .

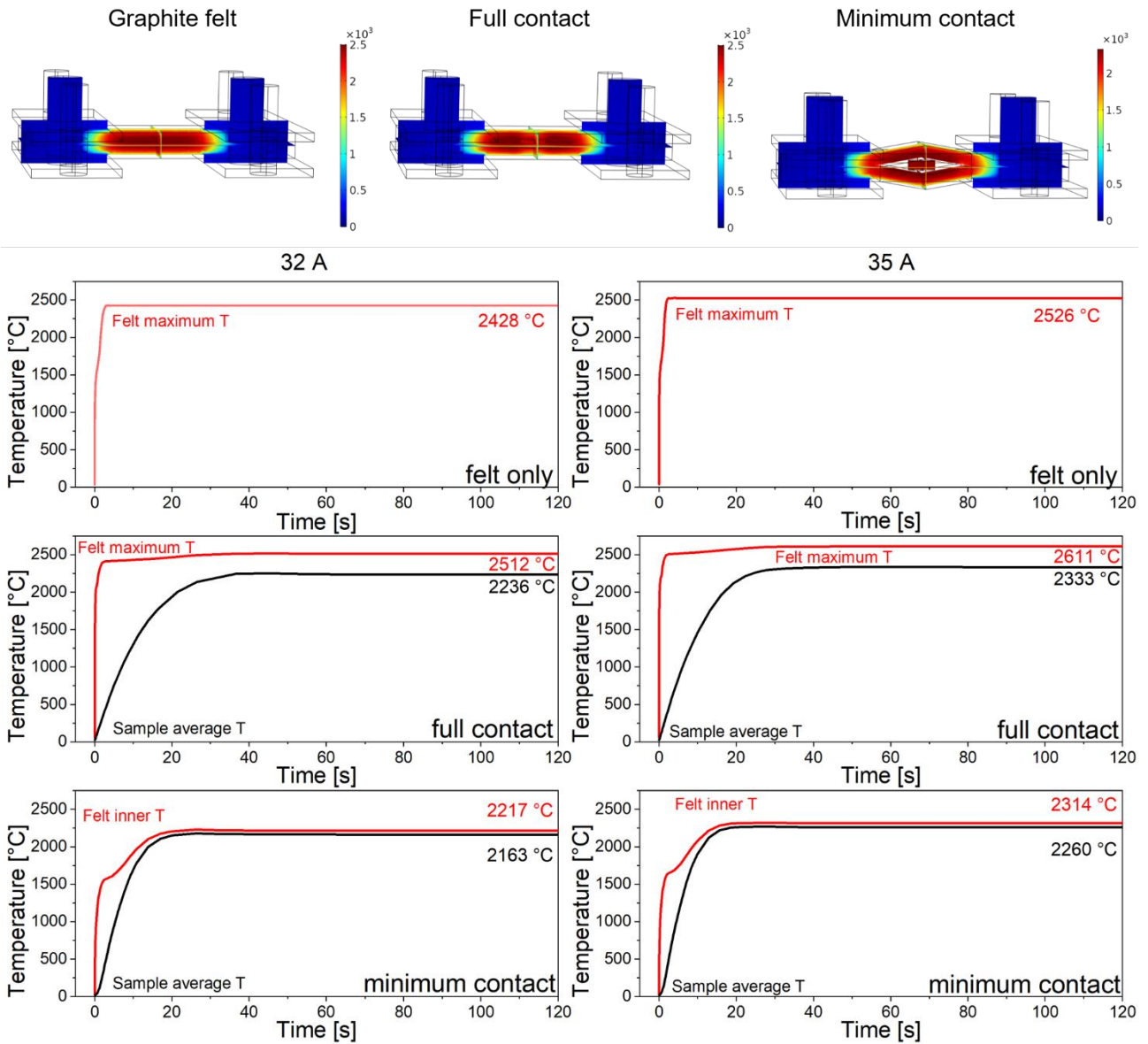


Figure 4: On the top, the three boundary conditions modeled for the temperature estimation: graphite felt without sample, graphite felt embedding the sample, and the sample placed within a hole in the graphite felt. On the bottom, the temperature profiles obtained by FEM of the three different geometries, for an applied current of 32 A and 35 A.

The maps recorded by EDXS on the samples obtained using the most “severe” conditions (35 A, 120 s) (**Figure 5**) confirm that the big equiaxial grains observed in the composite are Zr-rich being associated to ZrB<sub>2</sub>. On the other hand, the “dark phase” does not contain substantial zirconium, thus indicating that it originates from molten boron carbide.

Remarkably, EDXS linescan on pure  $ZrB_2$  samples also revealed the presence of limited secondary grain boundary phase, rich in uranium (**Figure 5**), not detectable by XRD. Uranium segregation has already been reported in hot-pressed  $ZrB_2$ - $B_4C$ -SiC by Neuman et al.[50], who observed the formation of different U-bearing phases for temperatures above 1600°C. In the present case, differently from the cited work, no Co or Fe could be detected in combination with U, but rather Y (**Figure S8** of the Supplementary material). The formation of U-enriched grain boundaries is not totally surprising as U and Zr have very similar oxide chemistry (same coordination, same valence and fluorite structures); therefore, small U contamination in Zr seems reasonable. The effect of this substantial modification of the grain boundary composition by massive impurities segregation on sintering and grain coarsening of  $ZrB_2$  has not been deeply investigated yet and could be a matter of future studies by UHS (which provides an effective tool to achieve ultra-high temperatures).

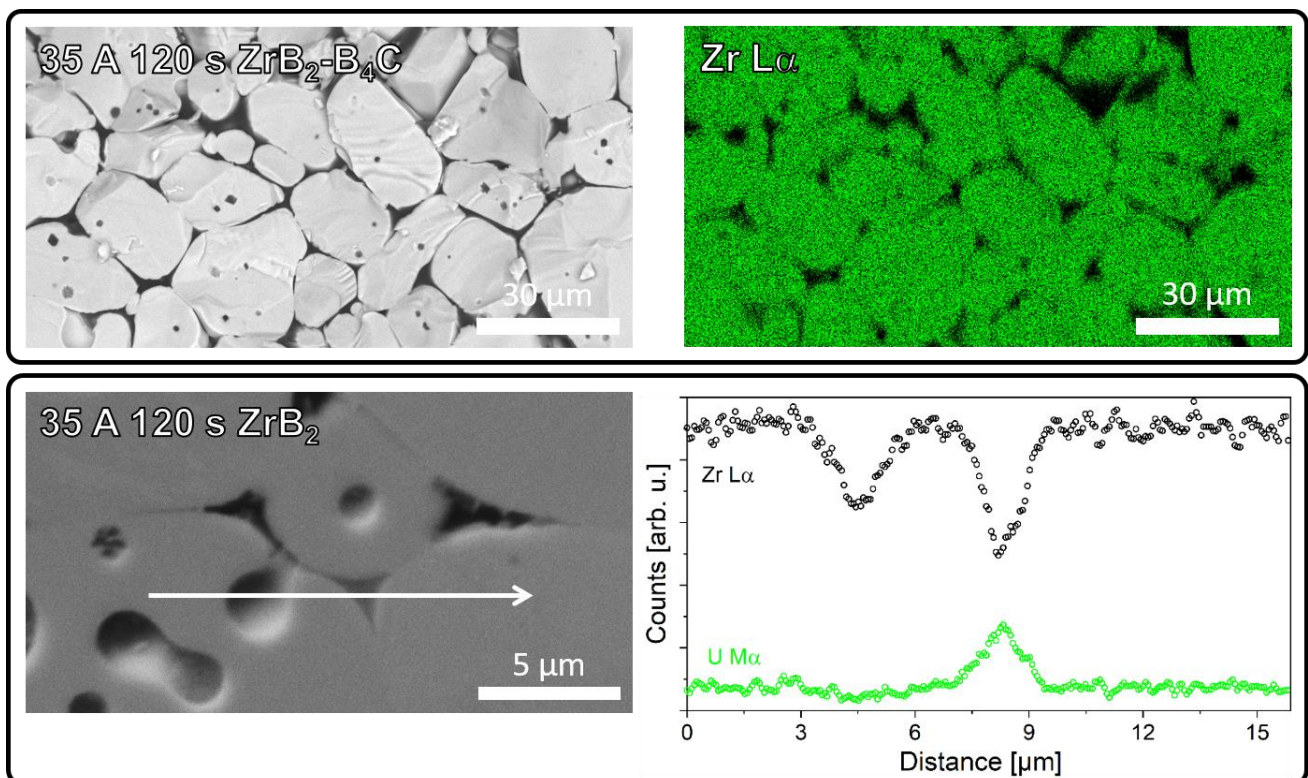


Figure 5: EDS mapping of UHSed  $ZrB_2$ - $B_4C$  sample produced at 35 A for 120 s (top panel); SEM micrograph and Zr- U linescan of pure  $ZrB_2$  sample UHSed in the same conditions (35 A for 120 s).

The Vickers hardness of the UHS samples was measured to qualitatively assess whether the mechanical properties of  $ZrB_2$  composites are comparable to that of materials produced by more conventional methods.

**Figure 6** shows the Vickers hardness of  $ZrB_2$  and  $ZrB_2-B_4C$  samples as a function of density. As expected, in the considered range hardness increases almost linearly with density, reaching the maximum value of 17.8 GPa for 97.5% dense  $ZrB_2-B_4C$  sample obtained using 35 A for 120 s.

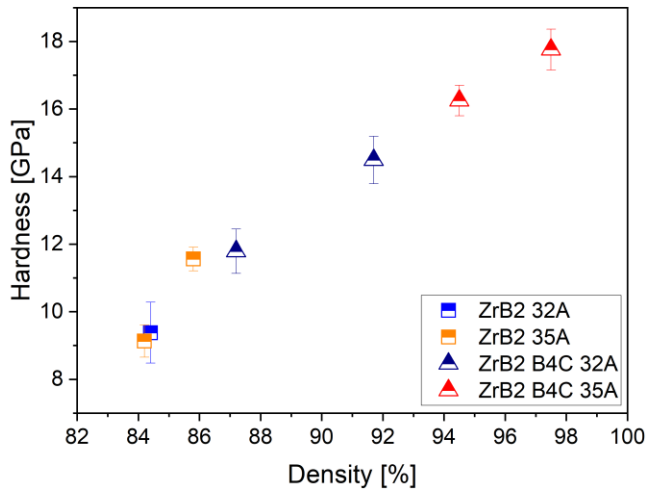


Figure 6: Vickers hardness of  $ZrB_2$  and  $ZrB_2-B_4C$  samples as a function of the density. Indents were performed with a load of 1 Kg, and only samples above 80 % were tested.

Some values from the literature, together with the results obtained in the present work, are summarized in **Table 2**. The hardness of  $ZrB_2-B_4C$  composites ranges between 15 and 20.5 GPa, depending final density achieved, and generally increasing with the  $B_4C$  content. Our values also fall in this range, showing performances comparable to those of  $ZrB_2-B_4C$  produced by SPS or even hot pressing. It is worth noting that, while these techniques generally result in finer grain size, they do not allow densification of complexly shaped objects. UHS therefore presents itself as an extremely convenient time- and energy-saving alternative for the consolidation of high-performance  $ZrB_2$ -based components.

Table 2: Vicker hardness (in GPa) values for  $ZrB_2$ -based samples of different densities and compositions available in the literature.

Source	Doping	Density [% TD ]	Hardness [GPa]	Produced by	Milled	Sintering conditions
Swab 2023[51]	1 % wt $B_4C$	>99	15.3	hot pressing	yes	2100 °C 30 min 32 MPa
Dorner 2021[52]	2 % vol $B_4C$	98	16.4	hot pressing	no	2100 °C 30 min 32 MPa

Chamberlain 2006[11]	3 % wt WC*	98	14.5	pressureless	yes	2150 °C 180 min
Fahrenholtz 2008[15]	4 % wt B <sub>4</sub> C	94	17.9	pressureless	no	1900 °C 120 min
Mandal 2022[48]	5 % wt B <sub>4</sub> C	96.1	15.4	SPS	no	2000 °C 15 min 50 MPa
	15 % wt B <sub>4</sub> C	97.5	16.3	SPS	no	2000 °C 15 min 50 MPa
	20 % wt B <sub>4</sub> C	97.7	18.9	SPS	no	2000 °C 15 min 50 MPa
	25 % wt B <sub>4</sub> C	97.8	20.5	SPS	no	2000 °C 15 min 50 MPa
This study	10 % wt B <sub>4</sub> C	97.5	17.8	UHS	no	35 A 120 s
	10 % wt B <sub>4</sub> C	94.5	16.3	UHS	no	35 A 60 s

\* contamination coming from wearing of the WC milling media.

## 4. Conclusions

Ultrafast high-temperature sintering (UHS) was used to densify commercial ZrB<sub>2</sub> powder, reaching maximum densities of 84.4 and 85.8% after 120 s under 32 and 35 A respectively. To overtake these values, 10%wt B<sub>4</sub>C was added to ZrB<sub>2</sub> as a sintering aid, resulting in 91.7 and 97.5% in the above-mentioned UHS conditions. When 32 A is applied, the addition of B<sub>4</sub>C efficiently enhances densification, likely due to the removal of the surface oxides present on the ZrB<sub>2</sub> particles. At 35 A, the temperature is high enough to lead to form a boron carbide-rich liquid phase, triggering liquid phase sintering. The Vickers hardness values measured on the UHS ZrB<sub>2</sub>-B<sub>4</sub>C samples are in line with values present in the literature, being equally or better than pressureless sintered or spark plasma sintered ZrB<sub>2</sub>-based components. The overall results prove that UHS is an effective tool to densify ultra-high temperature ceramics within a few minutes time scale.

## 5. Acknowledgments

The work was supported by the project PAT (AI) H2@TN through the fund SAP40104237 and by the Italian Ministry of Economic Development (Ministero dello Sviluppo Economico, MISE) within the project “Processo Innovativo per la Ceramica Tecnica - PRINCE”, F/310085/01/X56.

## References

- [1] W.G. Fahrenholtz, G.E. Hilmas, I.G. Talmy, J.A. Zaykoski, Refractory Diborides of Zirconium and Hafnium, *J. Am. Ceram. Soc.* 90 (2007) 1347–1364. <https://doi.org/10.1111/j.1551-2916.2007.01583.x>.
- [2] A.L. Chamberlain, W.G. Fahrenholtz, G.E. Hilmas, D.T. Ellerby, High-Strength Zirconium Diboride-Based Ceramics, *J. Am. Ceram. Soc.* 87 (2004) 1170–1172. <https://doi.org/10.1111/j.1551-2916.2004.01170.x>.
- [3] R.A. Cutler, S.J. Schneider, Engineered materials handbook, *Ceram. Glas.* 4 (1991) 787–803.
- [4] R. Telle, L.S. Sigl, K. Takagi, Boride-Based Hard Materials, in: *Handb. Ceram. Hard Mater.*, Wiley-VCH Verlag GmbH, Weinheim, Germany, n.d.: pp. 802–945. <https://doi.org/10.1002/9783527618217.ch22>.
- [5] F. Monteverde, S. Guicciardi, A. Bellosi, Advances in microstructure and mechanical properties of zirconium diboride based ceramics, *Mater. Sci. Eng. A.* 346 (2003) 310–319. [https://doi.org/10.1016/S0921-5093\(02\)00520-8](https://doi.org/10.1016/S0921-5093(02)00520-8).
- [6] R.A. Andrievskii, L.A. Korolev, V. V. Klimentko, A.G. Lanin, I.I. Spivak, I.L. Taubin, Effect of zirconium carbide and carbon additions on some physicochemical properties of zirconium diboride, *Sov. Powder Metall. Met. Ceram.* 19 (1980) 93–94. <https://doi.org/10.1007/BF00792032>.
- [7] D. KALISH, E. V. CLOUGHERTY, K. KREDER, Strength, Fracture Mode, and Thermal Stress Resistance of HfB<sub>2</sub> and ZrB<sub>2</sub>, *J. Am. Ceram. Soc.* 52 (1969) 30–36. <https://doi.org/10.1111/j.1151-2916.1969.tb12655.x>.
- [8] E. Zapata-Solvas, D.D. Jayaseelan, H.T. Lin, P. Brown, W.E. Lee, Mechanical properties of ZrB<sub>2</sub>- and HfB<sub>2</sub>-based ultra-high temperature ceramics fabricated by spark plasma sintering, *J. Eur. Ceram. Soc.* 33 (2013) 1373–1386. <https://doi.org/10.1016/j.jeurceramsoc.2012.12.009>.
- [9] S. Grasso, T. Saunders, H. Porwal, O. Cedillos-Barraza, D.D. Jayaseelan, W.E. Lee, M.J. Reece, Flash spark plasma sintering (FSPS) of pure ZrB<sub>2</sub>, *J. Am. Ceram. Soc.* 97 (2014) 2405–2408. <https://doi.org/10.1111/jace.13109>.
- [10] V.M. Gropyanov, Effect of dispersion on powder sintering, *Refractories.* 10 (1969) 769–775. <https://doi.org/10.1007/BF01290536>.
- [11] A.L. Chamberlain, W.G. Fahrenholtz, G.E. Hilmas, Pressureless Sintering of Zirconium Diboride, *J. Am. Ceram. Soc.* 89 (2006) 450–456. <https://doi.org/10.1111/j.1551-2916.2005.00739.x>.
- [12] S.C. Zhang, G.E. Hilmas, W.G. Fahrenholtz, Pressureless Densification of Zirconium Diboride with Boron Carbide Additions, *J. Am. Ceram. Soc.* 89 (2006) 1544–1550. <https://doi.org/10.1111/j.1551-2916.2006.00949.x>.
- [13] S. Zhu, W.G. Fahrenholtz, G.E. Hilmas, S.C. Zhang, Pressureless sintering of carbon-coated zirconium diboride powders, *Mater. Sci. Eng. A.* 459 (2007) 167–171. <https://doi.org/10.1016/j.msea.2007.02.116>.
- [14] S. Zhu, W.G. Fahrenholtz, G.E. Hilmas, S.C. Zhang, Pressureless Sintering of Zirconium Diboride Using Boron Carbide and Carbon Additions, *J. Am. Ceram. Soc.* 90 (2007) 3660–3663. <https://doi.org/10.1111/j.1551-2916.2007.01936.x>.
- [15] W.G. Fahrenholtz, G.E. Hilmas, S.C. Zhang, S. Zhu, Pressureless Sintering of Zirconium Diboride: Particle Size and Additive Effects, *J. Am. Ceram. Soc.* 91 (2008) 1398–1404. <https://doi.org/10.1111/j.1551-2916.2007.02169.x>.
- [16] D. Sciti, S. Guicciardi, A. Bellosi, G. Pezzotti, Properties of a Pressureless-Sintered ZrB<sub>2</sub>-MoSi<sub>2</sub> Ceramic Composite, *J. Am. Ceram. Soc.* (2006) 060427083300081-??? <https://doi.org/10.1111/j.1551-2916.2006.00999.x>.
- [17] F. Monteverde, A. Bellosi, S. Guicciardi, Processing and properties of zirconium diboride-based composites, *J. Eur. Ceram. Soc.* 22 (2002) 279–288. [https://doi.org/10.1016/S0955-2219\(01\)00284-9](https://doi.org/10.1016/S0955-2219(01)00284-9).
- [18] S.K. Mishra, S.K. Das, A.K. Ray, P. Ramachandrarao, Effect of Fe and Cr Addition on the Sintering Behavior of ZrB<sub>2</sub> Produced by Self-Propagating High-Temperature Synthesis, *J. Am. Ceram. Soc.* 85 (2004) 2846–2848. <https://doi.org/10.1111/j.1151-2916.2002.tb00540.x>.
- [19] E. Rudy, S. Windisch, No Title, Part II. Ternary Syst. Vol. XIII Phase Diagrams Syst. Ti-B-C, Zr-B-C Hf-B-C. Ternary Phase Equilibria Transit. Met. Syst. Rep. No. AFMLTR-65-2. Contract No. USAF 33(615). (1966) 183–188.
- [20] H.-B. Ma, H.-L. Liu, J. Zhao, F.-F. Xu, G.-J. Zhang, Pressureless sintering, mechanical properties and oxidation behavior of ZrB<sub>2</sub> ceramics doped with B<sub>4</sub>C, *J. Eur. Ceram. Soc.* 35 (2015) 2699–2705. <https://doi.org/10.1016/j.jeurceramsoc.2015.03.030>.
- [21] C. Wang, W. Ping, Q. Bai, H. Cui, R. Hensleigh, R. Wang, A.H. Brozena, Z. Xu, J. Dai, Y. Pei, C. Zheng, G. Pastel, J. Gao, X. Wang, H. Wang, J.-C. Zhao, B. Yang, X. (Rayne) Zheng, J. Luo, Y. Mo, B. Dunn, L. Hu, A general method to synthesize and sinter bulk ceramics in seconds, *Science* (80-. ). 368 (2020) 521–526. <https://doi.org/10.1126/science.aaz7681>.

- [22] F. Zuo, Q. Wang, Z.Q. Yan, M. Kermani, S. Grasso, G.L. Nie, B.B. Jiang, F.P. He, H.T. Lin, L.G. Wang, Upscaling Ultrafast High-Temperature Sintering (UHS) to consolidate large-sized and complex-shaped ceramics, *Scr. Mater.* 221 (2022) 114973. <https://doi.org/10.1016/j.scriptamat.2022.114973>.
- [23] R.-F. Guo, H.-R. Mao, Z.-T. Zhao, P. Shen, Ultrafast high-temperature sintering of bulk oxides, *Scr. Mater.* 193 (2021) 103–107. <https://doi.org/10.1016/j.scriptamat.2020.10.045>.
- [24] M. Biesuz, A. Galotta, A. Motta, M. Kermani, S. Grasso, J. Vontorová, V. Tyrpekl, M. Vilémová, V.M. Sglavo, Speedy bioceramics: Rapid densification of tricalcium phosphate by ultrafast high-temperature sintering, *Mater. Sci. Eng. C.* 127 (2021) 112246. <https://doi.org/10.1016/j.msec.2021.112246>.
- [25] M. Kermani, D. Zhu, J. Li, J. Wu, Y. Lin, Z. Dai, C. Hu, S. Grasso, Ultra-fast High-temperature Sintering (UHS) of translucent alumina, *Open Ceram.* 9 (2022) 100202. <https://doi.org/10.1016/j.oceram.2021.100202>.
- [26] L. Spiridigliozzi, G. Dell'Agli, S. Esposito, P. Rivolo, S. Grasso, V.M. Sglavo, M. Biesuz, Ultra-fast high-temperature sintering (UHS) of Ce<sub>0.2</sub>Zr<sub>0.2</sub>Y<sub>0.2</sub>Gd<sub>0.2</sub>La<sub>0.2</sub>O<sub>2-δ</sub> fluorite-structured entropy-stabilized oxide (F-ESO), *Scr. Mater.* 214 (2022) 114655. <https://doi.org/10.1016/j.scriptamat.2022.114655>.
- [27] T.P. Mishra, S. Wang, C. Lenser, D. Jennings, M. Kindelmann, W. Rheinheimer, C. Broeckmann, M. Bram, O. Guillon, Ultrafast high-temperature sintering of strontium titanate, *Acta Mater.* 231 (2022) 117918. <https://doi.org/10.1016/j.actamat.2022.117918>.
- [28] J. Wu, Y. Lin, M. Kermani, C. Hu, S. Grasso, Ultra-fast high temperature sintering (UHS) of Li<sub>1.5</sub>Al<sub>0.5</sub>Ge<sub>1.5</sub>P<sub>3</sub>O<sub>12</sub> electrolyte: A rationalization of the heating schedule, *Ceram. Int.* (2021). <https://doi.org/10.1016/j.ceramint.2021.11.178>.
- [29] A. Kern, P.J. McGinn, Ultrafast high-temperature sintering of Li<sub>7</sub>La<sub>3</sub>Zr<sub>1.75</sub>Nb<sub>0.25</sub>Al<sub>0.15</sub>O<sub>12</sub> (LLZO), *J. Eur. Ceram. Soc.* 42 (2022) 7501–7507. <https://doi.org/10.1016/j.jeurceramsoc.2022.08.054>.
- [30] F. Ye, F. Meng, T. Luo, H. Qi, Ultrafast high-temperature sintering of high-entropy (La<sub>0.2</sub>Nd<sub>0.2</sub>Sm<sub>0.2</sub>Eu<sub>0.2</sub>Gd<sub>0.2</sub>)<sub>2</sub>Hf<sub>2</sub>O<sub>7</sub> ceramics with fluorite structure, *Ceram. Int.* 48 (2022) 35649–35654. <https://doi.org/10.1016/j.ceramint.2022.09.041>.
- [31] M. Ihrig, T.P. Mishra, W.S. Scheld, G. Häuschen, W. Rheinheimer, M. Bram, M. Finsterbusch, O. Guillon, Li<sub>7</sub>La<sub>3</sub>Zr<sub>2</sub>O<sub>12</sub> solid electrolyte sintered by the ultrafast high-temperature method, *J. Eur. Ceram. Soc.* 41 (2021) 6075–6079. <https://doi.org/10.1016/j.jeurceramsoc.2021.05.041>.
- [32] Z. Lin, X. Zhao, C. Wang, Q. Dong, J. Qian, G. Zhang, A.H. Brozena, X. Wang, S. He, W. Ping, G. Chen, Y. Pei, C. Zheng, B.C. Clifford, M. Hong, Y. Wu, B. Yang, J. Luo, P. Albertus, L. Hu, Rapid Pressureless Sintering of Glasses, *Small.* 18 (2022) 2107951. <https://doi.org/10.1002/sml.202107951>.
- [33] H.-R. Mao, E.-T. Dong, S.-B. Jin, X.-M. Qiu, P. Shen, Ultrafast high-temperature synthesis and densification of high-entropy carbides, *J. Eur. Ceram. Soc.* 42 (2022) 4053–4065. <https://doi.org/10.1016/j.jeurceramsoc.2022.03.054>.
- [34] H.W. Li, Y.P. Zhao, G.Q. Chen, M.H. Li, Z.F. Wei, X.S. Fu, W.L. Zhou, SiC-based ceramics with remarkable electrical conductivity prepared by ultrafast high-temperature sintering, *J. Eur. Ceram. Soc.* (2022). <https://doi.org/10.1016/j.jeurceramsoc.2022.12.025>.
- [35] R.-X. Luo, M. Kermani, Z.-L. Guo, J. Dong, C.-F. Hu, F. Zuo, S. Grasso, B.-B. Jiang, G.-L. Nie, Z.-Q. Yan, Q. Wang, Y.-L. Gan, F.-P. He, H.-T. Lin, Ultrafast high-temperature sintering of silicon nitride: A comparison with the state-of-the-art techniques, *J. Eur. Ceram. Soc.* 41 (2021) 6338–6345. <https://doi.org/10.1016/j.jeurceramsoc.2021.06.021>.
- [36] H. Xie, M. Qin, M. Hong, J. Rao, M. Guo, J. Luo, L. Hu, Rapid liquid phase-assisted ultrahigh-temperature sintering of high-entropy ceramic composites, *Sci. Adv.* 8 (2022). <https://doi.org/10.1126/sciadv.abn8241>.
- [37] M. Patel, V.V.B. Prasad, V. Jayaram, Heat conduction mechanisms in hot pressed ZrB<sub>2</sub> and ZrB<sub>2</sub>-SiC composites, *J. Eur. Ceram. Soc.* 33 (2013) 1615–1624. <https://doi.org/10.1016/j.jeurceramsoc.2013.03.006>.
- [38] M. Rahman, C.C. Wang, W. Chen, S.A. Akbar, C. Mroz, Electrical Resistivity of Titanium Diboride and Zirconium Diboride, *J. Am. Ceram. Soc.* 78 (1995) 1380–1382. <https://doi.org/10.1111/j.1151-2916.1995.tb08498.x>.
- [39] W. Tan, C.A. Petorak, R.W. Trice, Rare-earth modified zirconium diboride high emissivity coatings for hypersonic applications, *J. Eur. Ceram. Soc.* 34 (2014) 1–11. <https://doi.org/10.1016/j.jeurceramsoc.2013.07.016>.
- [40] S. Mandal, A. Pramanick, S. Chakraborty, P. Pratim Dey, Phase determination of ZrB<sub>2</sub>-B<sub>4</sub>C ceramic composite material using XRD and rietveld refinement analysis, *Mater. Today Proc.* 33 (2020) 5664–5666. <https://doi.org/10.1016/j.matpr.2020.04.124>.
- [41] V. Petříček, M. Dušek, L. Palatinus, Crystallographic Computing System JANA2006: General features, *Zeitschrift Für Krist. - Cryst. Mater.* 229 (2014) 345. <https://doi.org/10.1515/zkri-2014-1737>.
- [42] W. Ji, B. Parker, S. Falco, J.Y. Zhang, Z.Y. Fu, R.I. Todd, Ultra-fast firing: Effect of heating rate on sintering of 3YSZ, with and

without an electric field, *J. Eur. Ceram. Soc.* 37 (2017) 2547–2551.

- [43] M. Biesuz, L. Spiridigliozzi, M. Frasnelli, G. Dell'Agli, V.M.V.M. Sglavo, Rapid densification of Samarium-doped Ceria ceramic with nanometric grain size at 900–1100°C, *Mater. Lett.* 190 (2017) 17–19. <https://doi.org/10.1016/j.matlet.2016.12.132>.
- [44] V. Esposito, E. Traversa, Design of electroceramics for solid oxides fuel cell applications: Playing with ceria, *J. Am. Ceram. Soc.* 91 (2008) 1037–1051. <https://doi.org/10.1111/j.1551-2916.2008.02347.x>.
- [45] M. Biesuz, S. Grasso, V.M. Sglavo, What's new in ceramics sintering? A short report on the latest trends and future prospects, *Curr. Opin. Solid State Mater. Sci.* 24 (2020) 100868. <https://doi.org/10.1016/j.cossms.2020.100868>.
- [46] W. Ji, J. Zhang, W. Wang, Z. Fu, R.I. Todd, The microstructural origin of rapid densification in 3YSZ during ultra-fast firing with or without an electric field, *J. Eur. Ceram. Soc.* 40 (2020) 5829–5836. <https://doi.org/10.1016/j.jeurceramsoc.2020.07.027>.
- [47] R.M. German, *Liquid phase sintering*, Springer Science, New York (USA), 1985.
- [48] S. Mandal, S. Chakraborty, P. Dey, A study of mechanical properties and WEDM machinability of spark plasma sintered ZrB<sub>2</sub>–B<sub>4</sub>C ceramic composites, *Micron.* 153 (2022) 103198. <https://doi.org/10.1016/j.micron.2021.103198>.
- [49] Y.-M. Chiang, D. Birnie, P.W.D. Kingery, *Physical Ceramics: Principles for Ceramic Science and Engineering*, Wiley, 1997.
- [50] E.W. Neuman, G.E. Hilmas, W.G. Fahrenholtz, Mechanical behavior of zirconium diboride–silicon carbide–boron carbide ceramics up to 2200°C, *J. Eur. Ceram. Soc.* 35 (2015) 463–476. <https://doi.org/10.1016/j.jeurceramsoc.2014.09.021>.
- [51] J.J. Swab, J. Jarman, W. Fahrenholtz, J. Watts, Mechanical properties of ZrB<sub>2</sub> ceramics determined by two laboratories, *Int. J. Appl. Ceram. Technol.* (2023). <https://doi.org/10.1111/ijac.14429>.
- [52] A.N. Dorner, K. Werbach, G.E. Hilmas, W.G. Fahrenholtz, Effect of tantalum solid solution additions on the mechanical behavior of ZrB<sub>2</sub>, *J. Eur. Ceram. Soc.* 41 (2021) 3219–3226. <https://doi.org/10.1016/j.jeurceramsoc.2020.12.049>.

## Supplementary material

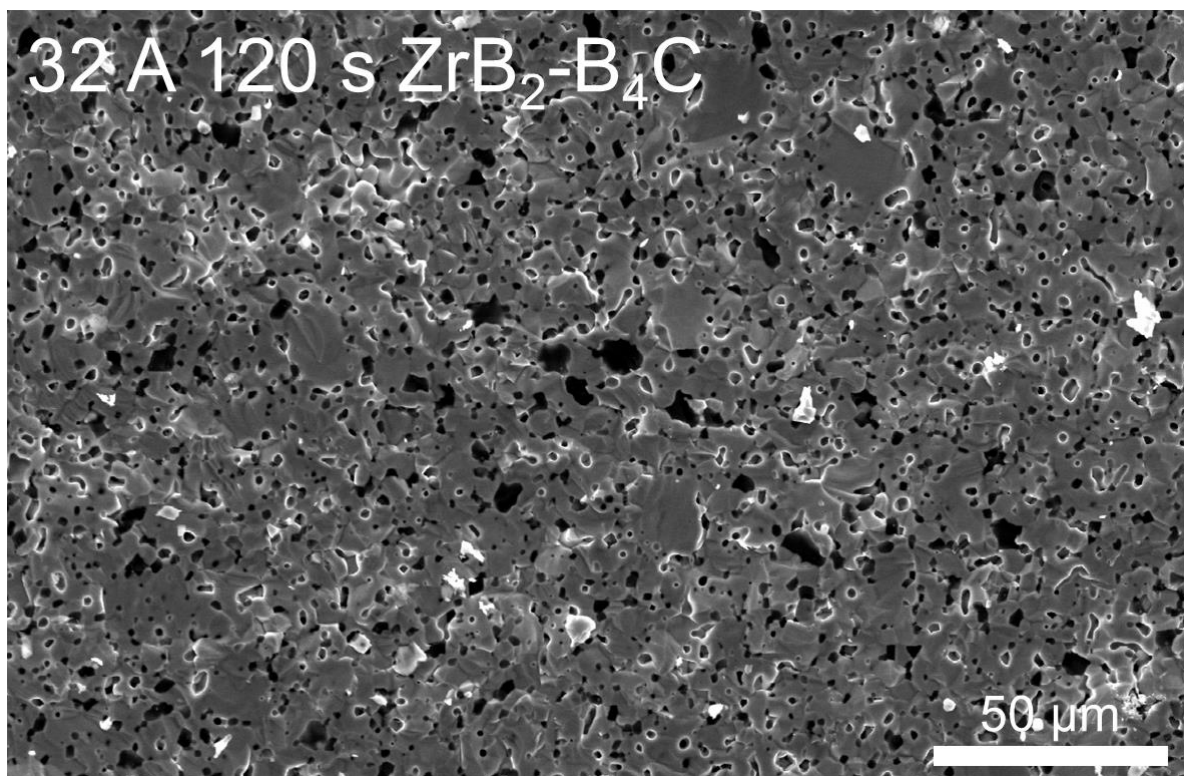


Figure S1: lower magnification SEM SE micrograph of the ZrB<sub>2</sub>-B<sub>4</sub>C sample treated at 32 A for 120 s.

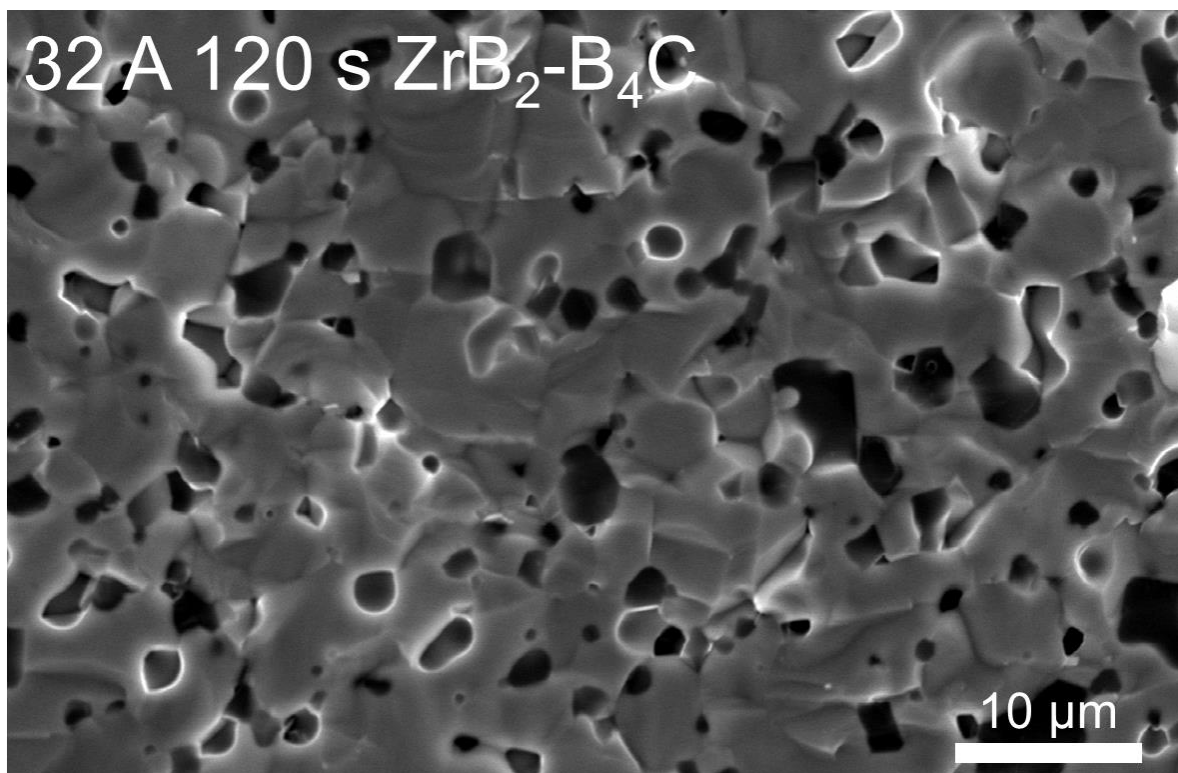


Figure S2: higher magnification SEM SE micrograph of the  $\text{ZrB}_2\text{-B}_4\text{C}$  sample treated at 32 A for 120 s.

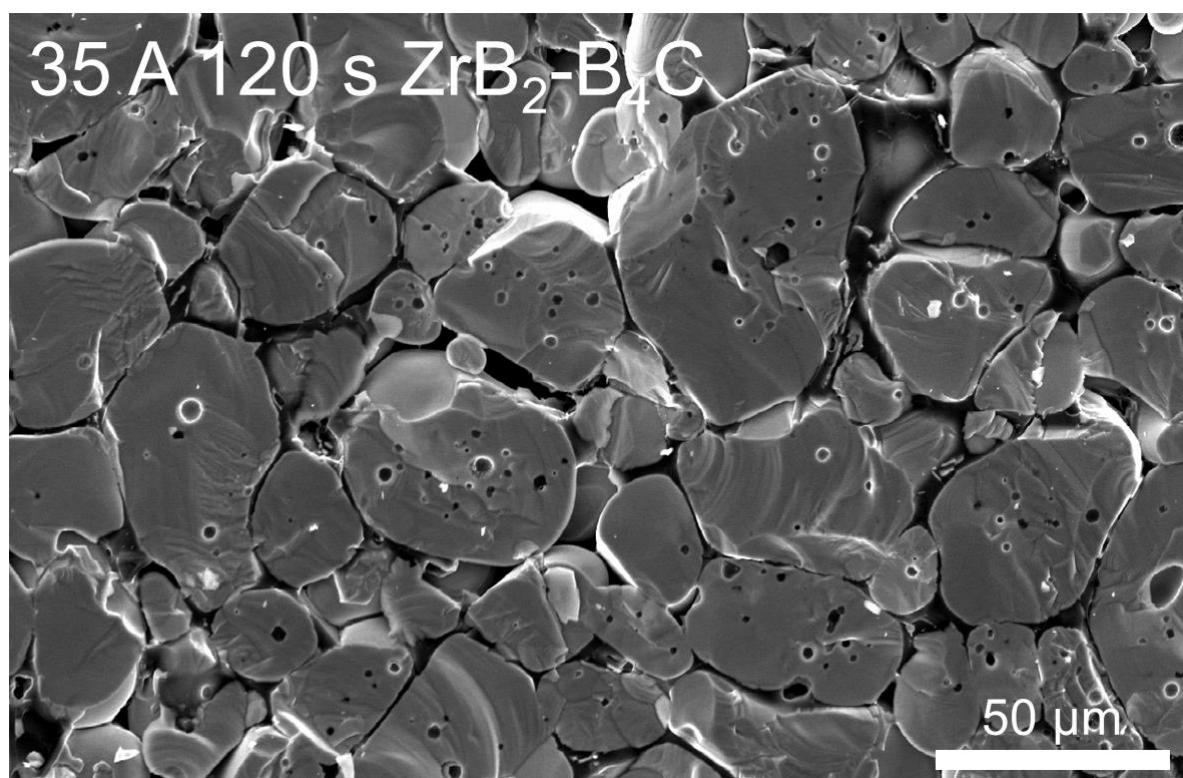


Figure S3: lower magnification SEM SE micrograph of the  $\text{ZrB}_2\text{-B}_4\text{C}$  sample treated at 35 A for 120 s.

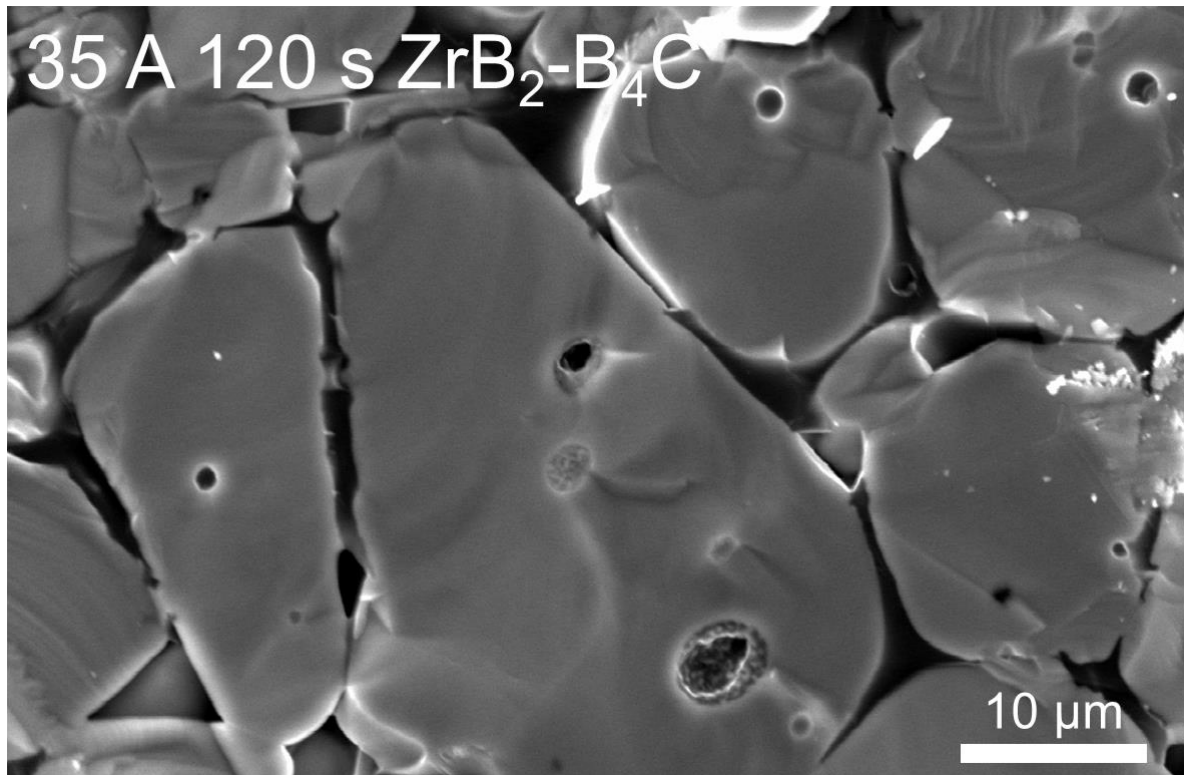


Figure S4: higher magnification SEM SE micrograph of the  $ZrB_2-B_4C$  sample treated at 35 A for 120 s.

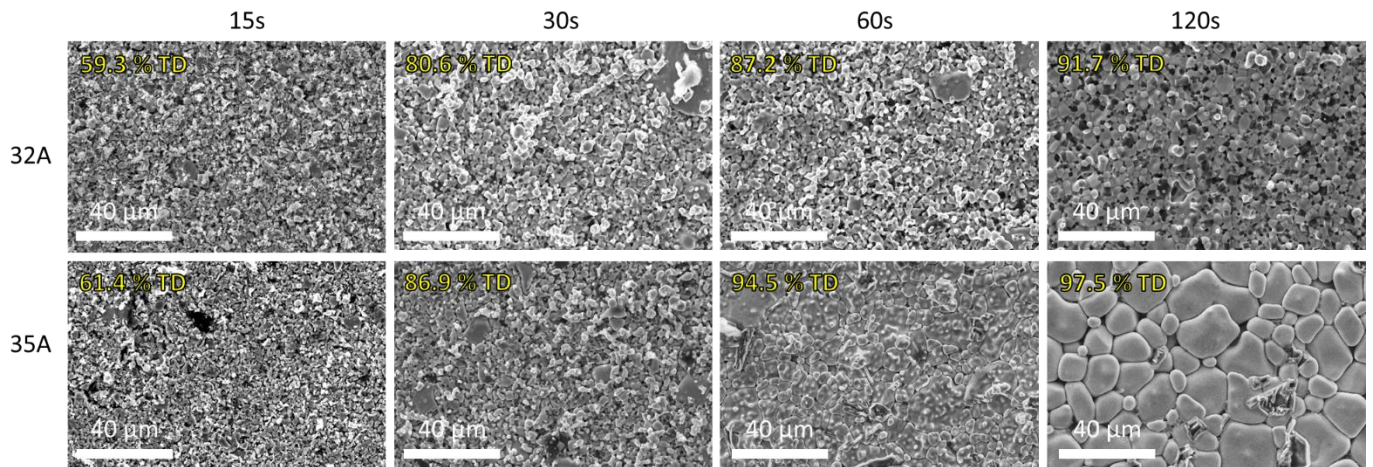


Figure S5: SEM SE micrographs of the outer surface of the  $ZrB_2-B_4C$  samples as function of the sintering conditions.

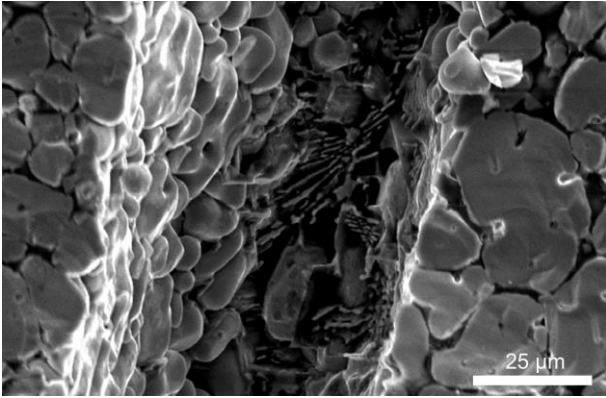


Figure S6: SEM SE image of a eutectic solidification structure found in a localized spot of the  $ZrB_2-B_4C$  sample treated sintered with 35 A for 120 s.

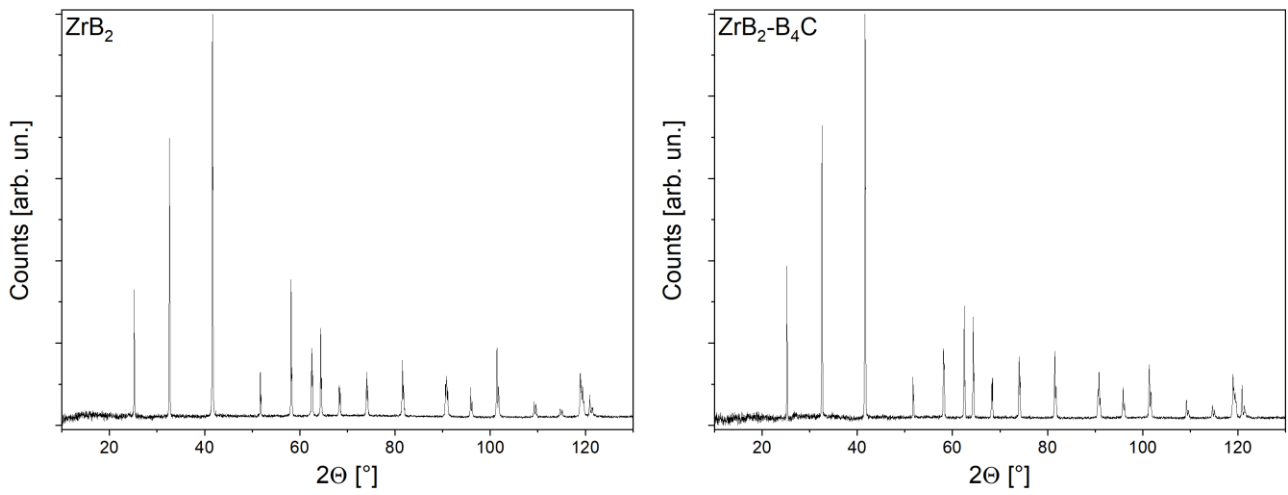


Figure S7: XRD patterns of the  $ZrB_2$  and  $ZrB_2-B_4C$  samples treated at 35 A for 120 s.

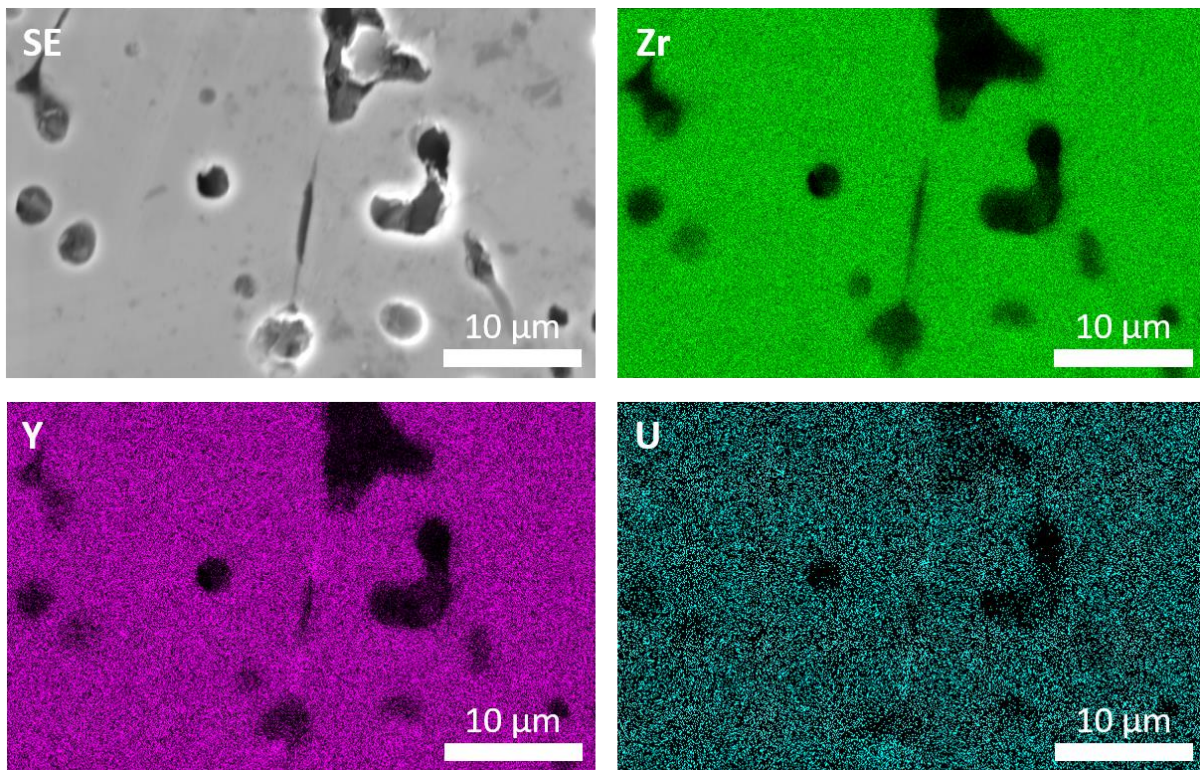


Figure S8: SEM BSE image and EDS mapping (Zr, Y, and U) of a U-rich region of the ZrB<sub>2</sub> sample treated with 35 A for 120 s.